Earth, Planets and Space

FULL PAPER

Source rupture process of the M_W 6.2 earthquake in the Noto Peninsula, central Japan, on May 5, 2023

Kimiyuki Asano[1*] and Tomotaka Iwata[2]

Abstract

An M_{JMA} 6.5 crustal earthquake occurred during earthquake swarm activity around the northeastern tip of the Noto Peninsula, central Japan, on May 5, 2023. To elucidate the position of this earthquake in the continuing seismic swarm activity, it is necessary to clarify the relationships between the source rupture process, crustal structure, and the earthquake swarm activity. The kinematic source rupture process of this event was analyzed using strong-motion waveform records observed at strong-motion stations surrounding the source region using the finite source inversion method, incorporating a three-dimensional velocity model in the target area. The rupture propagated mainly in the up-dip direction on a source fault plane dipping southeastward at an angle of 40°. A significant slip with a maximum slip amount of 0.8 m was found in the depth range of 8–11 km, which is approximately 4 km in the up-dip direction from the hypocenter. The slip direction was thrust type, with a small right-lateral strike-slip component. The location of this asperity corresponded to the region of low V_P/V_S ratio. The total seismic moment was 2.40×10^{18} Nm (M_W 6.2). Most slips occurred at depths shallower than those of the preceding seismic activity, which occurred primarily at depths from 10 to 14 km. The seismic activity immediately after this earthquake occurred around the large-slip area, with intensive earthquakes occurring at shallow depths (< 10 km). Active seismic activity in and around the rupture area of the M_W 6.2 earthquake on May 5, 2023, continued intensively even after this earthquake, and then the rupture of the 2024 Noto Hanto earthquake (M_{JMA} 7.6) on January 1, 2024, started at the southwestern edge of the asperity of the M_W 6.2 earthquake. Therefore, this earthquake can be interpreted as one of turning point in this earthquake swarm activity to connect the preceding swarm in the depth range from 10 to 15 km with seismic activity in shallower depths including the further destructive event.

Keywords 2023 Noto Peninsula earthquake, Source rupture process, Kinematic source inversion, Strong motion data, Earthquake swarm

*Correspondence:
Kimiyuki Asano
k-asano@sms.dpri.kyoto-u.ac.jp
Full list of author information is available at the end of the article

Graphical Abstract

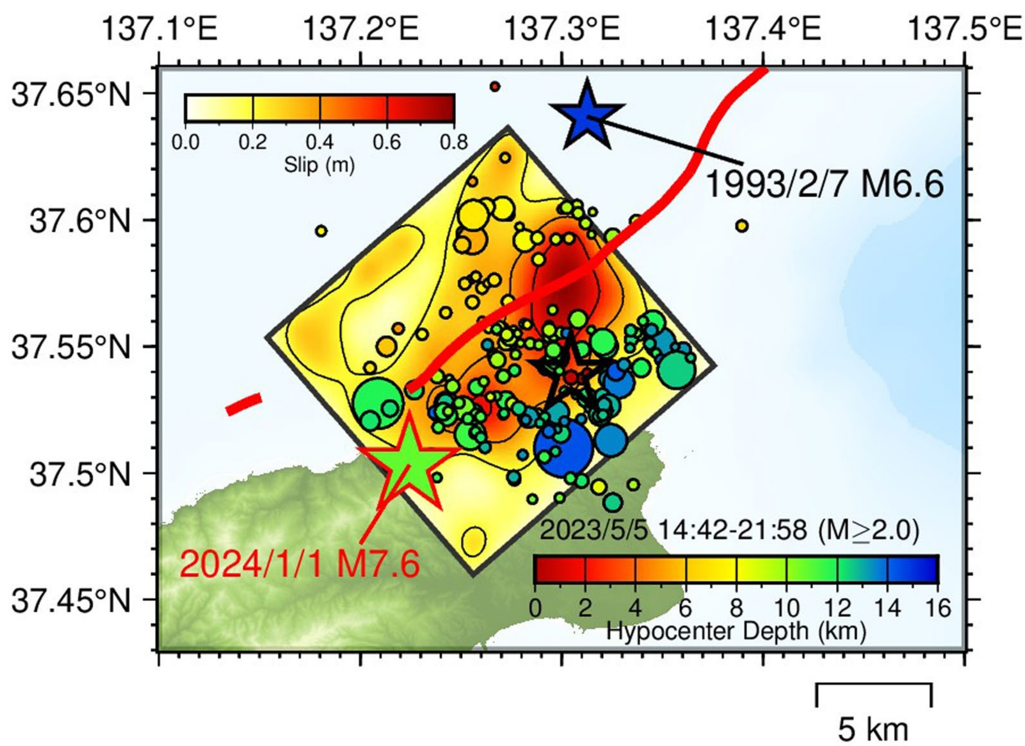

1 Introduction

Earthquake swarm activity has been intense for more than 3 years since December 2020 around the northeastern tip of the Noto Peninsula, central Japan. This earthquake swarm consists of four seismic clusters, and their spatiotemporal characteristics were investigated in terms of the diffusive migration of hypocenters driven by the fluid supply (Amezawa et al. 2023; Kato 2024; Nishimura et al. 2023; Yoshida et al. 2023b). According to Amezawa et al. (2023), the earthquake swarm activity started in the southern cluster (S cluster in their paper) located near the southern coast of the Noto Peninsula, and the subsequent intense activity started in other three clusters distributed west, north, and northeast of the southern cluster. Details of the spatio-temporal swarm activity in each cluster can be found in the above-mentioned papers.

Most of the earthquakes in each cluster were distributed over a depth range of 10–15 km in the crust until May 5, 2023. Subsequently, an earthquake with an M_{JMA} of 6.5 occurred at a depth of 12.1 km near the northeast coast of the Noto Peninsula in the northeast cluster of earthquakes at 14:42:04.10 JST (5:42:04.10 UTC) on May 5, 2023 (Fig. 1). The earthquake was the largest event of the swarm. After the occurrence of M_{JMA} 6.5 earthquake, small earthquakes became widespread at shallower depths of 5–10 km (Yoshida et al. 2023a). This seismic activity was followed by a devastating M_{JMA} 7.6 earthquake on January 1, 2024, called the 2024 Noto Hanto earthquake (e.g., Yoshida et al. 2024).

Seafloor active faults around the Noto Peninsula were identified using ocean-floor seismic profiling (e.g., Inoue and Okamura 2010; Ishiyama et al. 2017). The earthquake on May 5, 2023, occurred near one of these seafloor active faults, the Suzu–oki segment (Inoue and Okamura 2010) or the NT5 fault (MEXT and ERI 2021; Sato et al. 2020). The Suzu–oki (NT5) fault is a southeast-dipping reverse fault. Thus, this earthquake drew particular attention to the relationship between the seafloor active faults and this event. The geometry of the source fault and its rupture process should be investigated to clarify this point.

To clarify the position of this earthquake in the ongoing seismic swarm activity, since it is the largest event at the time of its occurrence, it is seismologically necessary to clarify the relationships between the heterogeneous source rupture process, the crustal structure, and the earthquake swarm activity. Therefore, this study focused on the rupture

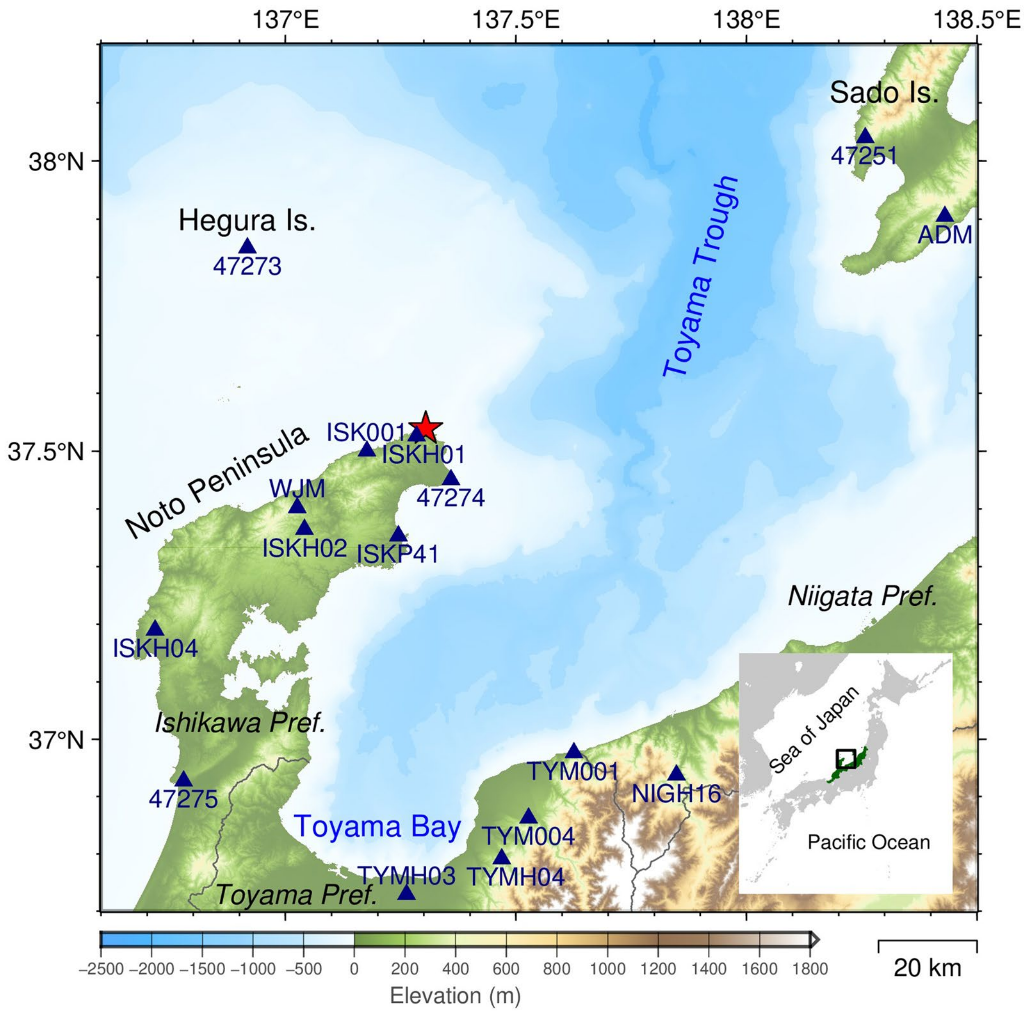

Fig. 1 Index map of the study area. The epicenter of the M_{JMA} 6.5 earthquake on May 5, 2023, located by JMA is represented by the red star (JMA 2023). Solid triangles indicate the locations of strong motion stations utilized for the kinematic finite source inversion analysis. The topography in land area is drawn using the 10 m mesh digital elevation model produced by the Geospatial Information Authority of Japan. The bathymetry is based on SYNBATH V2.0 (Sandwell et al. 2022). The gray lines represent the prefectural boundaries. The inset map shows the location of the study area in the Japanese Islands. The dark green area indicates the Hokuriku region

process of the source fault during the M_{JMA} 6.5 earthquake. The source rupture process was analyzed by kinematic waveform inversion of strong-motion waveforms. A three-dimensional velocity model was used to compute the theoretical Green's functions, considering the complex underground structures of this region, including thick Neogene and Quaternary sediments. Finally, the relationships between the rupture process, seafloor active faults, crustal structure, and seismic activity are discussed.

2 Methods and data

2.1 Kinematic finite source inversion

The kinematic source rupture process of the earthquake was estimated using the linear waveform inversion method with multiple time windows (Hartzell and Heaton 1983; Olson and Apsel 1982). This inversion scheme solves the observational equation based on the representation theorem (Burridge and Knopoff 1964; Maruyama 1963). This technique has been applied to many earthquakes in earlier studies (e.g., Asano and Iwata 2019, 2021; Ma et al. 2001; Sekiguchi et al. 2000; Wald and Heaton 1994; Yoshida et al. 1996).

A planar fault model is used to represent the source fault of the earthquake. Considering the variety of seismic moment tensor solutions routinely determined by various Japanese and overseas organizations, strike and dip angles were searched during the inversion process. Therefore, the strike and dip angles were searched among six (41°, 45°, 49°, 53°, 57°, and 61°), and seven (25°, 30°, 35°, 40°, 45°, 50°, and 55°) cases, respectively. The length and width of the assumed fault plane were 14 and 18 km, respectively, after preliminary analysis. The assumed fault plane was divided into small sub-faults (2×2 km) along the strike and dip directions. The rupture starting point was fixed at the hypocenter (37.5390°N, 137.3045°E, depth 12.14 km) located by the Japan Meteorological Agency (JMA). Recently, Yoshida et al. (2024) published the relocated catalog of this earthquake swarm, and the location of the hypocenter in their relocated catalog was 37.53658°N, 137.30161°E at a depth of 12.24 km. The spatial difference of the hypocenter between the JMA catalog and Yoshida et al. (2024) for this earthquake is much smaller than the sub-fault size used in this study.

A point source was assigned at the center of each sub-fault, and the moment-rate function of each sub-fault was represented by the superposition of several time windows. The basis function of each time window is given by a bell-shaped source-time function. The duration of each time window is 0.8 s, and each successive time window is time-shifted by 0.4 s. We assigned six time windows for each sub-fault after a preliminary analysis. The rupture of the first time window was triggered at the time of rupture, assuming circular rupture propagation at a constant velocity initiated from the hypocenter. The spatiotemporal smoothing constraint among the unknown parameters was introduced following the way proposed by Sekiguchi et al. (2000). The best strike and dip angles were selected together with the relative weight of the smoothing constraint by minimizing Akaike's Bayesian Information Criterion (ABIC) (Akaike 1980; Fukahata and Wright 2008). The variation in the rake angle was limited to within $90^\circ \pm 45^\circ$ using the nonnegative least squares method (Lawson and Hanson 1974).

2.2 Strong motion waveform data

The observed strong motion waveform data were collected from the nationwide observation network MOWLAS (Monitoring of Waves on Land and Seafloor) of NIED (K-NET, KiK-net, and F-net) and the seismic intensity observation networks of the JMA and Ishikawa Prefectural Government. Sixteen strong-motion stations were selected considering the azimuthal coverage, site conditions, and data quality (Fig. 1). We used strong-motion waveform records from the downhole sensor for the NIED KiK-net stations, records from the sensor installed in the observatory vault of the NIED F-net stations, and records on the ground surface of the other stations.

The original data are ground acceleration data, except for the NIED F-net stations, which are equipped with velocity-type strong motion sensors (Aoi et al. 2020). The three components of the acceleration time histories were integrated into the velocity in the time domain and bandpass filtered between 0.05 and 1 Hz. Subsequently, all waveform data were resampled at 10 Hz. We used the time segment from 1 to 15 s before and after the S-wave onset at each station, respectively.

2.3 Green's functions based on a three-dimensional velocity model

Thick Neogene and Quaternary sediments exist in the Hokuriku region (e.g., Ito et al. 2016). The velocity structures in the sedimentary layers are rather complex because of the back-arc rift structure formed during the opening of the Sea of Japan during the Neogene period and the compression caused by the subduction of the Pacific Plate beneath the Japanese archipelago (Ishiyama et al. 2017; Sato 1994). We used several stations more than 100 km away from the epicenter to improve azimuthal coverage. However, a one-dimensional velocity model may not accurately reproduce the wave propagation in such a distance range for shallow earthquakes in some cases (Shimomoto and Kakehi 2023). Therefore, the theoretical Green's function, which accounts for seismic wave propagation from the source to a station, was prepared based on a three-dimensional velocity model for this region. Development of detailed velocity models in many countries in recent decades enable us to utilize realistic three-dimensional velocity models in finite source inversion studies (e.g., Asano and Iwata 2019; Gallovič et al. 2015; Guo et al. 2013; Kubo et al. 2016; Lee et al. 2023; Somala et al. 2018; Yun et al. 2016).

The theoretical Green's functions were computed using the staggered-grid finite difference method (FDM) in Cartesian coordinates, which solves the elastodynamic wave equation in a velocity–stress formulation with fourth-order accuracy in space and second-order accuracy in time using the Fortran code developed and used in Asano et al. (2016). The Japan Integrated Velocity Structure Model (JIVSM) version 1, a nationwide three-dimensional velocity model released by the Headquarters for Earthquake Research Promotion (HERP) of the Japanese government, was used to compute the theoretical Green's functions. This velocity model is composed of many isotropic homogeneous velocity layers down to the upper mantle. Each of the layer boundaries was modeled simultaneously and sequentially using various types of data sets, such as extensive refraction/reflection experiments, gravity surveys, surface geology, borehole logging data, microtremor surveys, and earthquake ground motion records (Koketsu et al. 2012). The lowest S-wave velocity V_S in this model was

350 m/s; however, it was 500 m/s in most areas of the target region. Figure S1 shows a map of the bedrock depth (top surface of $V_S = 3.2$ km/s) and the vertical cross section of the S-wave velocity of the JIVSM, including the hypocenter. The bedrock along the Toyama Trough was relatively deep.

The reciprocal Green's function technique was used to reduce the computational cost (Eisner and Clayton 2001; Graves and Wald 2001). As we tested 42 combinations of strike and dip angles, as explained above, the reciprocal technique is indispensable for completing this study within a realistic timeframe. Figure S2 shows a comparison of the forward and reciprocal Green's functions. The source assumed for this verification was a double-couple point source located at the hypocenter with pure dip slip. This comparison confirms that the reciprocal Green's function technique works satisfactorily in the 3D ground motion simulation.

The FDM space comprised an area of 170 km (E–W) × 170 km (N–S), corresponding to the geographical area, as shown in Fig. S1, and extended to a depth of 40 km below the ground surface. The FDM space was discretized using a uniform grid (0.05 km along each Cartesian axis. Thus, the total number of FDM grid points is 9,276,574,402. The time step in the FDM calculation was set to 0.0025 s to satisfy the stability condition of the staggered-grid FDM scheme. The resultant Green's functions were filtered and resampled in the same manner as the observed records.

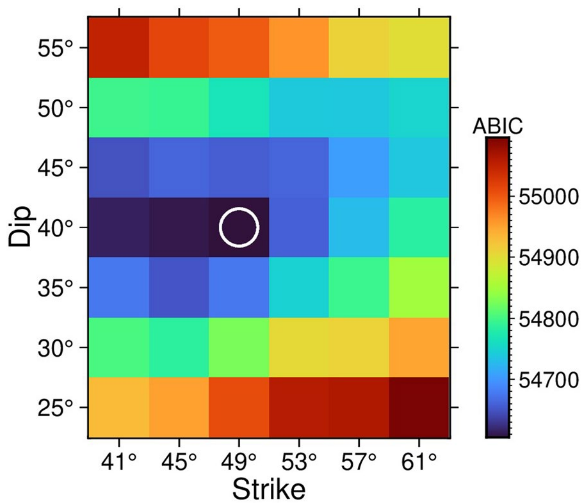

Fig. 2 Matrix plot of ABIC value for different strike and dip angles. The white circle indicates the minimum ABIC

3 Results

A strike angle of 49° and dip angle of 40° were selected as the best fault geometries based on the ABIC, as indicated in Fig. 2. This fault geometry correlates well with the early aftershock distribution based on the relocated hypocenter catalog by Yoshida et al. (2024) (Fig. 3). This comparison confirmed that the kinematic source inversion using strong motion data has enough capability to determine the fault geometry. However, the seafloor-active fault NT5 in this region did not match with that of the source fault of the earthquake (Fig. 3). The dip angle is also lower than that of the NT5 fault, although the strike angle is close to that of the NT5 fault (52°). Therefore, it can be concluded that this earthquake ruptured another blind fault located deeper than NT5.

The final slip distribution and moment-rate function of each sub-fault are shown in Fig. 4. The fault slip was a thrust motion with a small right-lateral strike-slip component. The largest slip (0.8 m) was found in a large-slip area (asperity) in the depth range of 8–11 km, which is at an up-dip of approximately 4 km from the hypocenter. The rupture propagated mainly in the up-dip direction (Fig. 5). The rupture of the asperity continued for approximately 5 s and the total rupture duration of the earthquake was approximately 8 s. The rupture propagation velocity of the first time-window was selected to be 2.3 km/s, which was 68% of the shear wave velocity at the source depth. The total seismic moment of the estimated source model is 2.40×10^{18} Nm, which corresponds to a moment magnitude M_W of 6.2. The average slip is 0.3 m.

A comparison of the observed and synthetic velocity waveforms is presented in Fig. 6. The model explained the overall features of the observed waveforms. The best set of strike and dip angles was determined based on ABIC as explained above. An additional comparison of synthetic velocity waveforms at six stations in the Noto Peninsula among three cases with different strike and dip angles is shown in Fig. S3. (strike, dip) = (49°, 40°) is the best case with the minimum ABIC value. On the other hand, the case of (strike, dip) = (61°, 25°) is the worst case among all the tested cases with the maximum ABIC value, and the case of (strike, dip) = (41°, 50°) is a moderate case. The minimum ABIC case (red traces in Fig. S3) looks the best in terms of waveform reproduction. The difference in waveforms from the moderate case (green traces in Fig. S3) is not significant, because difference of strike and dip angles is not large, but the initial part of the S-wave at about 1.5 s in the east–west component at WJM of NIED F-net, where the site condition is relatively good, because the sensor is installed in an observatory tunnel in mountain, does not match the characteristics of the observed waveform such as polarity even in the moderate case possibly due to inconsistency of the focal mechanism. The maximum ABIC case (blue trace in Fig. S3) looks the worst among the three cases. In particular, the amplitude of ISK001 is quite small. Therefore, the

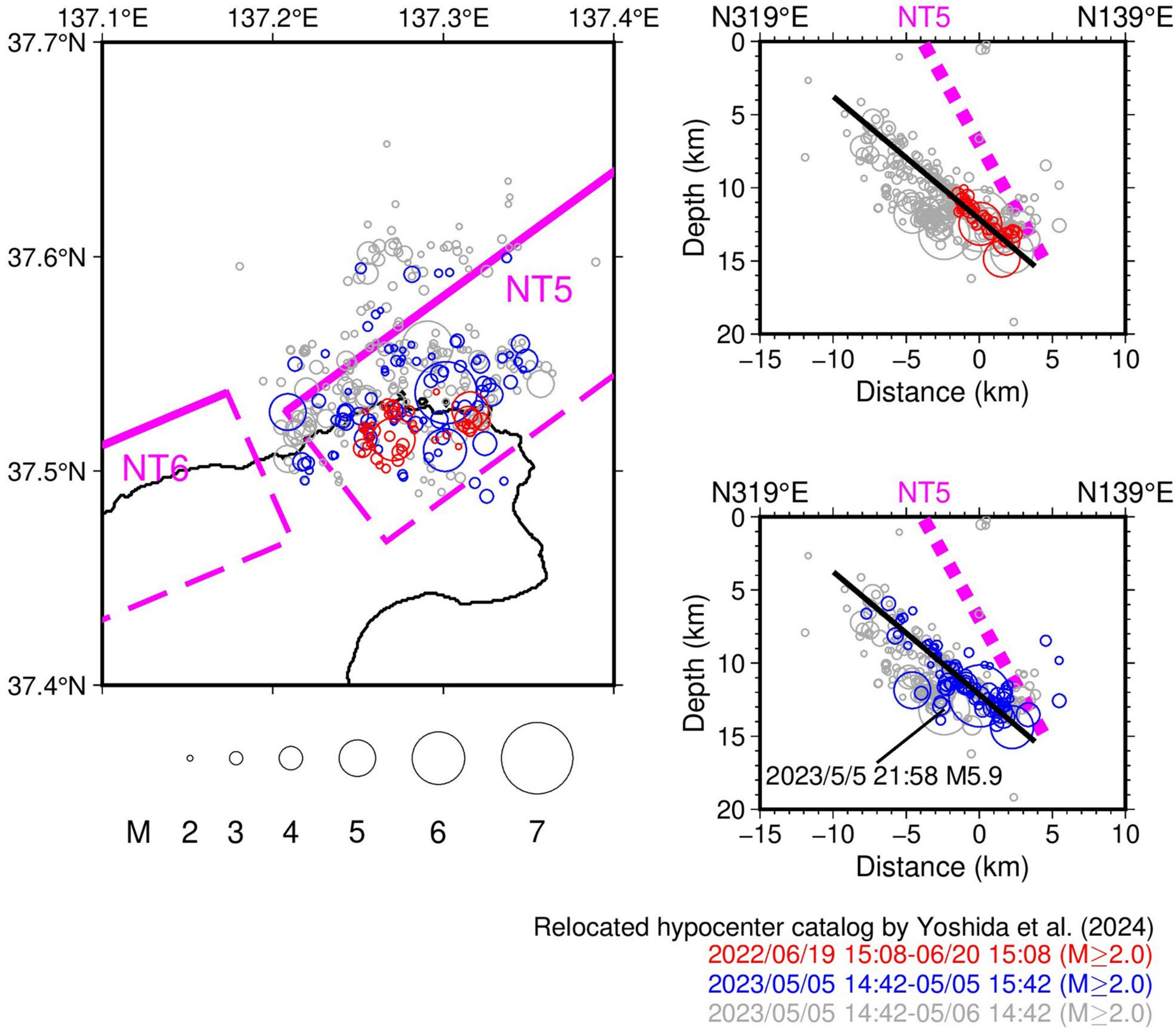

Fig. 3 Map view and vertical cross sections of hypocenters (open circles) in three different periods and the estimated source fault plane (black solid line). The earthquakes larger than M 2.0 in Yoshida et al. (2024) within 10 km across the cross section are plotted. The purple broken line in the cross sections represents the NT5 fault reported by MEXT and ERI (2021) and Sato et al. (2020)

authors believe that the ABIC approach worked well in this problem. Nevertheless, further updates of the three-dimensional velocity model may be necessary to improve the waveform fit at some stations, such as ISKH01 and ISKP41 in the Noto Peninsula and TYM004 and TYMH04 in the Toyama Plain.

4 Discussion

4.1 Spatial correlation with heterogeneous seismic velocity structure

It is crucial for evaluating seismic hazards to investigate the relationship between the fault rupture process and crustal structure. To observe the spatial correlation with the heterogeneous crustal seismic velocity structure, the slip distribution is plotted in Fig. 7 together with the seismic velocity model (V_P, V_S, and V_P/V_S) obtained from the seismic tomography analysis by Matsubara et al. (2022). Matsubara et al. (2022) performed seismic tomography for the entire Japanese archipelago, including the Sea of Japan and the Pacific Ocean, using arrival times from both the reflection surveys and the routine seismic network. The horizontal grid spacing in their tomography model is 0.1° (approximately 10 km), and the vertical grid spacing is 2.5 km (depth < 10 km) or 5 km (10 km < depth < 40 km). In particular, they successfully imaged the crust at shallow depth along the Sea of Japan,

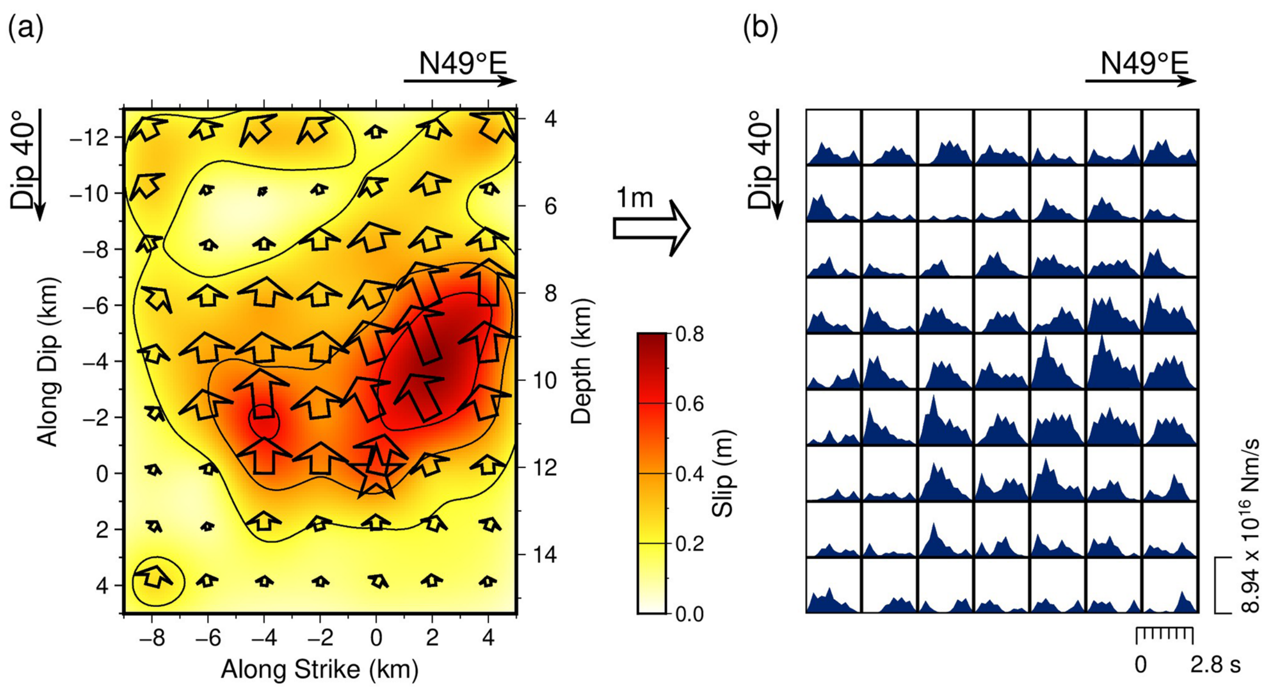

Fig. 4 Source model of the M_W 6.2 earthquake in the Noto Peninsula on May 5, 2023. **a** Spatial distribution of the final slips on the assumed fault plane with a contour interval of 0.2 m. The open star indicates the hypocenter or the rupture starting point. The arrow shows the slip vector of the hanging wall relative to the foot wall. **b** Estimated moment rate functions of each sub-fault

including the offshore area around the Noto Peninsula and Sado Island, using airgun data in the Sea of Japan. Thus, their velocity model is good for us to compare the fault slip and crustal heterogeneity in this region. Although we should keep in mind the spatial resolution of the seismic tomography model, we mainly focus on spatial change in the velocity structure along the dip direction on the source fault. The asperity or large-slip area correlates with the low V_P/V_S region (< 1.7), which suggests strong coupling of the asperity before the earthquake at these depths. This asperity is also located within the seismogenic zone ($V_P \sim 6.0$ km/s) in the region.

The final slip distribution shown in Fig. 4a is consistent with that of another study of the same earthquake by Yoshida et al. (2023a), who estimated the slip distribution by inverting the apparent moment rate functions obtained by deconvolving the observed waveforms of 21 Japanese broadband seismic stations (NIED F-net) using an empirical Green's function. Therefore, we think that this spatial correlation between the asperity of this earthquake and the low V_P/V_S region might be robust. However, the rupture did not expand northeastward, although the low V_P/V_S region in Matsubara et al. (2022) extended northeastward outside the source fault of this M_W 6.2 event. As discussed in the next subsection, there is a possibility that the fault segment northeast of this earthquake was ruptured during an M_{JMA} 6.6 earthquake on February 7, 1993, or an M_{JMA} 7.6 earthquake on January 1, 2024. Rupture growth to the northeast during the M_W 6.2 earthquake on May 5, 2023, might be limited by fault segmentation, small-scale heterogeneity, or past seismic activity, etc.

The spatial relationship between heterogeneous fault slip and three-dimensional velocity structure has also been investigated in many studies of past inland crustal earthquakes in Japan (e.g., Hori et al. 2006; Okada et al. 2007a, b, 2012; Shito et al. 2017). For example, Okada et al. (2012) investigated the spatial relationship between the heterogeneous fault slip and three-dimensional velocity structure based on their analysis for the 2008 Iwate–Miyagi Nairiku earthquake (M_{JMA} 7.2) in northeast Japan and many previous studies for other crustal earthquakes. They summarized that large coseismic slip areas have been estimated in higher velocity regions in the upper crust. They discussed that such a high-velocity area might act as asperity that can store large strain and generate large slip. Therefore, Okada et al. (2012) and their related studies mainly focused on the comparison between the coseismic slip and the spatial variation in the seismic velocity itself, but they have also pointed out that the low V_P/V_S ratio in the low-velocity region around faults in the upper crust could be interpreted as the area of relatively high aspect ratio pore with free aqueous fluids. These previous findings suggest that we should

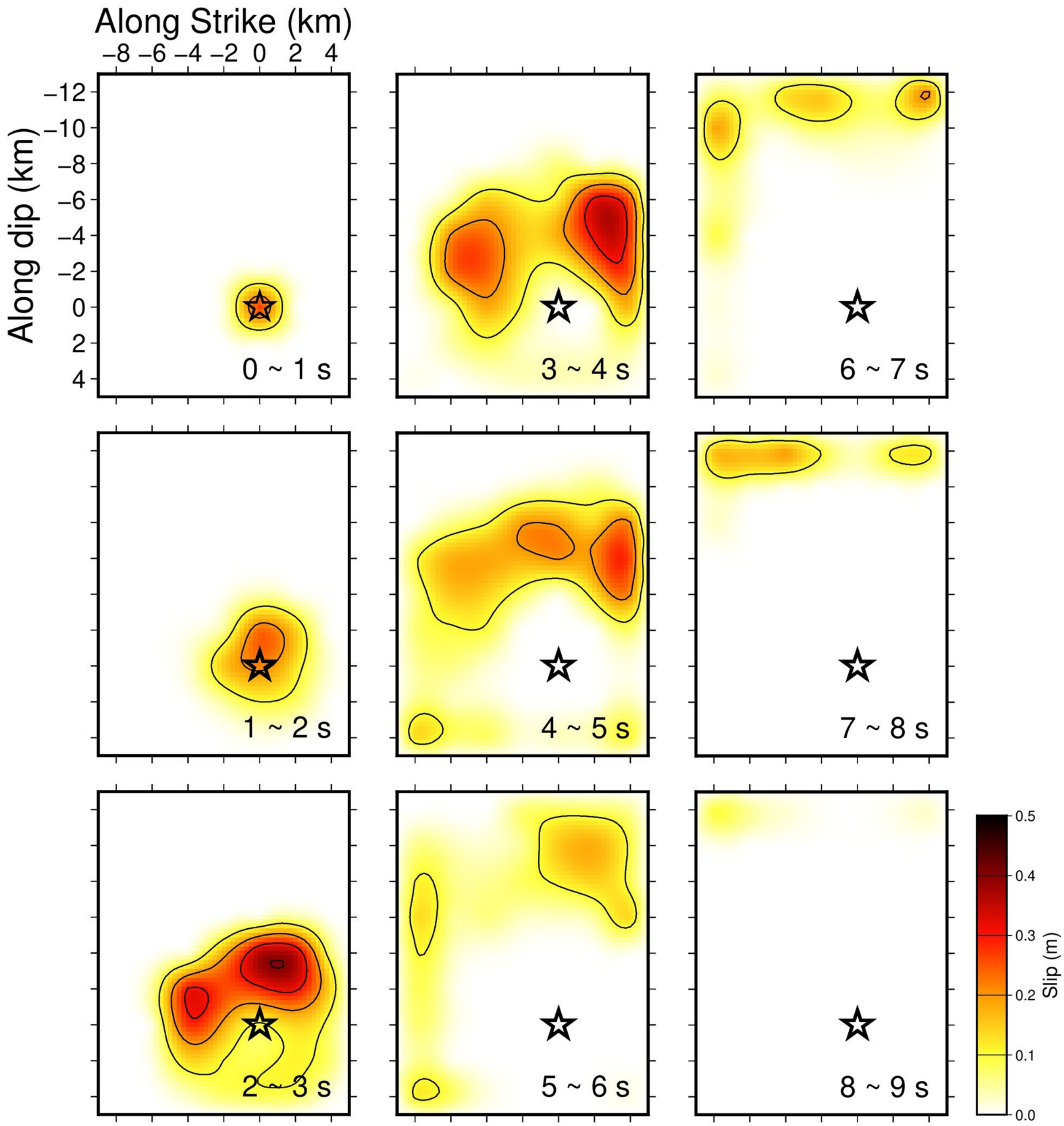

Fig. 5 Snapshots of the temporal slip progression at every 1 s. The open star denotes the rupture starting point

look at both the absolute seismic velocity and the V_P/V_S ratio to understand the seismogenic nature of the crust.

Hori et al. (2006) found that the large-slip area of the 2005 West off Fukuoka earthquake (M_{JMA} 7.0) corresponded to the high-velocity region and considered that a high-velocity medium has high strength. However, they reported that the V_P/V_S ratio in the large-slip area in the high-velocity medium was not low because of the complex elastic medium in the region. Their result on the V_P/V_S ratio is not similar to our result for M_W 6.2 earthquake in the Noto Peninsula on May 5, 2023, possibly because of the difference in the complexity of the crustal material. On the contrary, Shito et al. (2017) reported that a large-slip area of the 2016 Kumamoto earthquake (M_{JMA} 7.3) corresponded to the region with moderate seismic velocities (V_P = 6.0 km/s, V_S = 3.5 km/s)

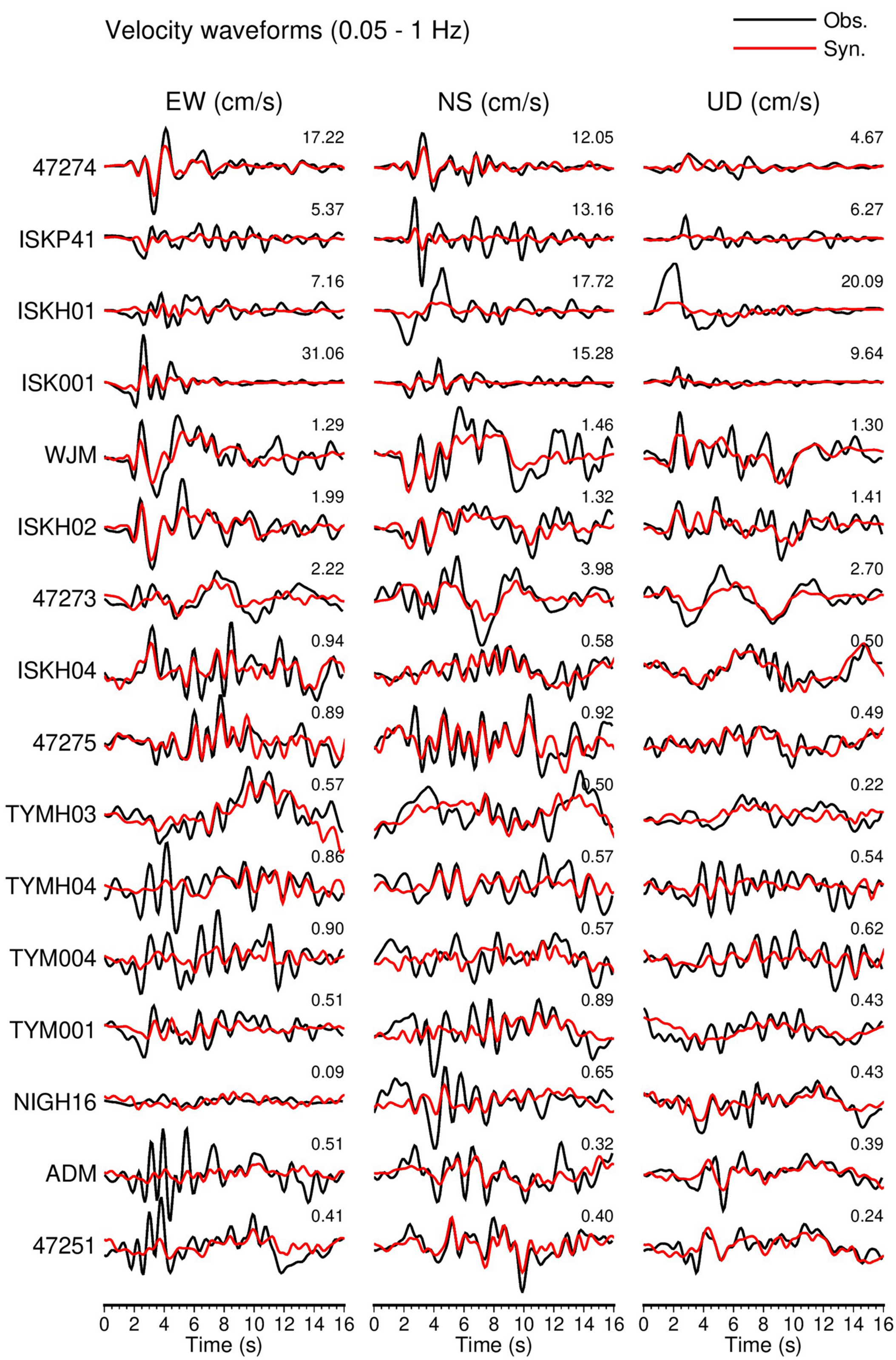

Fig. 6 Comparison of the observed velocity waveforms (black traces) and the synthetic velocity waveforms (red traces) in 0.05–1 Hz. The amplitudes were normalized by the maximum observed amplitude of each station. The maximum observed amplitude of each component is shown above each trace in units of cm/s. NS north–south, EW east–west, UD up–down

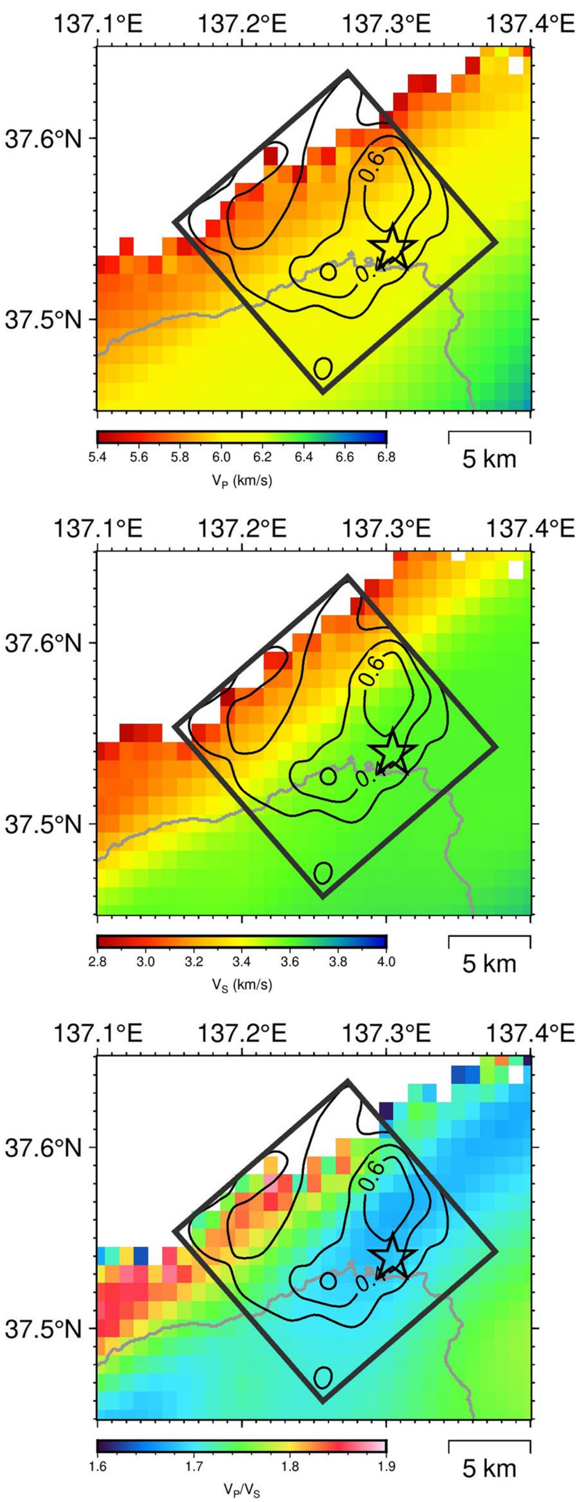

Fig. 7 Comparison between the slip distribution and seismic velocity structure by Matsubara et al. (2022) in the depth range along the source fault plane. (Top) P-wave velocity (V_P), (middle) S-wave velocity (V_S), (bottom) V_P/V_S ratio

and $V_P/V_S < 1.73$. Similarly, the asperity of the M_W 6.2 earthquake on May 5, 2023, also lies in the region of such seismic velocities and V_P/V_S ratio (Fig. 7).

In view of the above discussions, the role of the three-dimensional heterogeneous velocity structure in the fault rupture process during large earthquakes should be studied in more detail by accumulating knowledge from such large crustal earthquakes. A higher resolution velocity model in the target area would help us to investigate the spatial relationship between rupture growth and the heterogeneous crustal structure.

4.2 Relationship with seismic activity

Figure 8 shows the spatial relationship between the slip distribution of the M_W 6.2 earthquake analyzed in this study and small earthquakes over three different time periods. The relocated hypocenter catalog of this earthquake swarm, produced by Yoshida et al. (2024), was used for the plots shown in Fig. 8a, b. The largest event in this earthquake swarm preceding the M_W 6.2 event on May 5, 2023, was an M_{JMA} 5.4 event that occurred on June 19, 2022, at a depth of 12.5 km (Fig. 8a). JMA (2023) determined the centroid moment tensor solution of the M_{JMA} 5.4 event on June 19, 2022, and the resulting nodal plane was (strike, dip, rake) = (64°, 42°, 99°), which showed that this earthquake had occurred on a southeast dipping fault plane with moderate dip angle similar to the M_W 6.2 earthquake on May 5, 2023. This earthquake and its aftershocks occurred primarily at depths of 10–14 km. The hypocenters of these aftershocks do not overlap with the area of significant slip during the M_W 6.2 earthquake, although the 2022 M_{JMA} 5.4 earthquake might share the same source fault plane as that of the 2023 M_W 6.2 earthquake (Fig. 3).

As presented in the Introduction section, seismic activity extended to shallower depths after the M_W 6.2 earthquake on May 5, 2023 (Kato 2024; Yoshida et al. 2023a). Most aftershocks within approximately 7 h of the M_W 6.2 event were distributed around the asperity (Fig. 8b). Such complementary distribution of aftershocks is common in many crustal earthquakes (e.g., Asano and Iwata 2011; Mendoza and Hartzell 1988; Shito et al. 2017). An immediate M_{JMA} 5.4 aftershock occurred 29.8 s after the M_W 6.2 earthquake at a depth of 14.6 km (JMA 2023) or 14.4 km (Yoshida et al. 2024) in the down-dip direction on the same fault plane, which is the opposite direction of the rupture propagation during the M_W 6.2 event. This fact suggests that the down-dip portion of the source fault ruptured by the M_{JMA} 5.4 aftershock with a delay of 30 s. Contrarily, the largest aftershock (M_{JMA} 5.9, M_W 5.7) occurred at 21:58:04 JST on the same day at a depth of 13.7 km (JMA 2023) or 13.2 km (Yoshida et al. 2024). This depth is approximately 4 km deep from

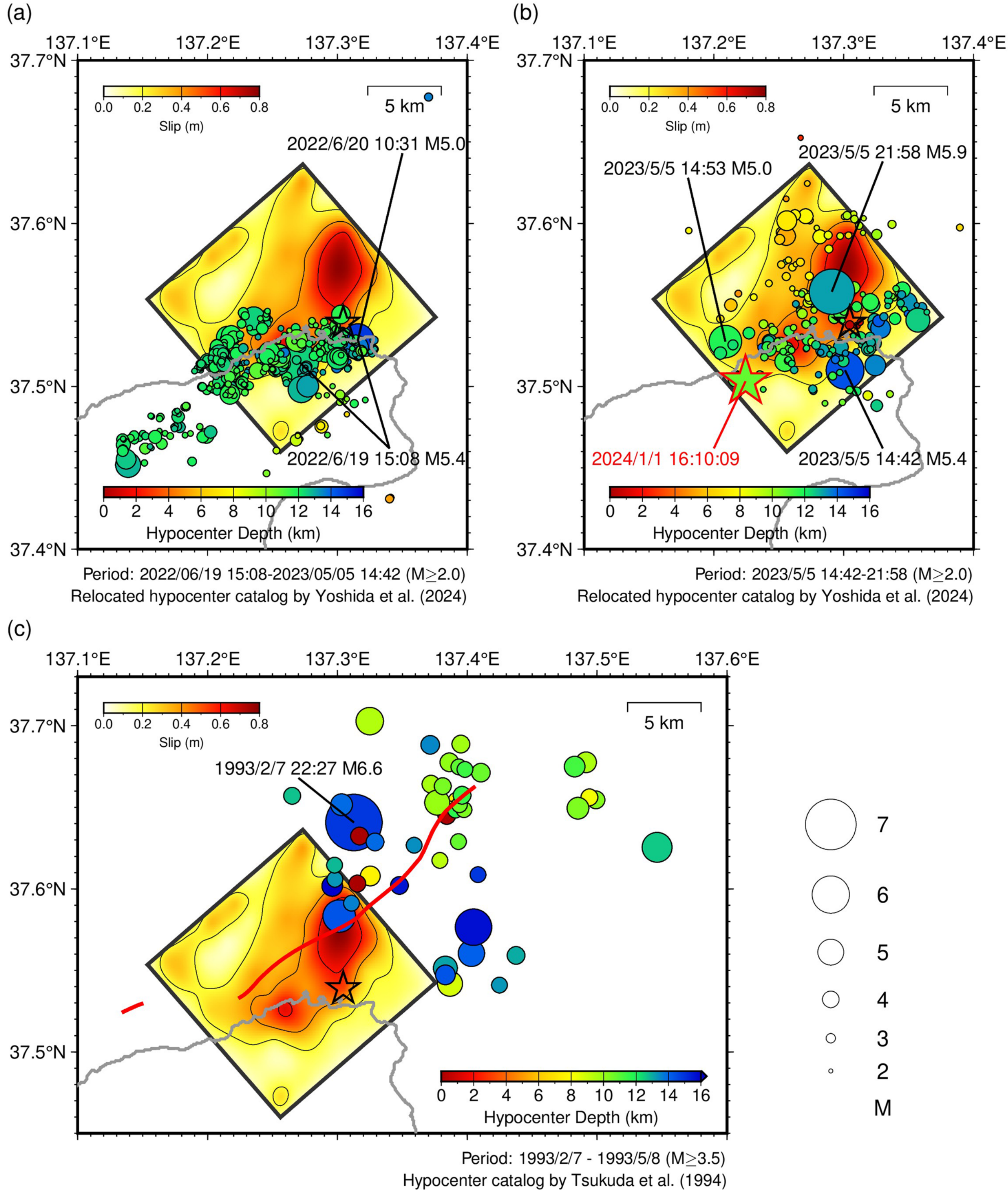

Fig. 8 Comparison of slip distribution and hypocenters in three different time periods. The open star indicates the epicenter of the M_W 6.2 earthquake on May 5, 2023. **a** Earthquakes (M ≥ 2.0) from 15:08 June 19, 2022 to 14:42 May 5, 2023 in the relocated hypocenter catalog of Yoshida et al. (2024). **b** Aftershocks (M ≥ 2.0) from 14:42 to 21:58 on May 5, 2023, in the relocated hypocenter catalog of Yoshida et al. (2024). **c** Mainshock and aftershocks (M ≥ 3.5) of the 1993 Off Noto Peninsula earthquake located by Tsukuda et al. (1994). Red lines represent the traces of seafloor active faults reported by Inoue and Okamura (2010)

the source fault plane of the M_W 6.2 event. Therefore, the largest aftershock may have ruptured another fault plane in the area (Kato 2024; Yoshida et al. 2023a).

Another remarkable earthquake occurred in this region. A large earthquake (M 6.6) occurred northeast of the Noto Peninsula on February 7, 1993 (hereafter, the 1993 Off Noto Peninsula earthquake). This was also a reverse-fault-type earthquake (Kamata and Takemura 1999; Tsukuda et al. 1994). Figure 8c shows the spatial distribution of the relocated hypocenters of earthquakes with magnitudes greater than 3.5 in a period from February 7 to May 8, 1993, published by Tsukuda et al. (1994). Most of the aftershocks occurred at depths of 10 to 15 km. Tsukuda et al. (1994) reported that the 1993 Off Noto Peninsula earthquake occurred on a fault plane dipping northwestward, considering the three-dimensional aftershock distribution, and concluded that the extension of the source fault plane of the 1993 Off Noto Peninsula earthquake did not coincide with any known seafloor active faults. Contrastingly, Kamata and Takemura (1999) proposed that a source fault model dipping southeastward is more plausible based on modeling long-period surface waves observed at local strong-motion stations. Regardless of the fault geometry, the aftershock distribution suggests that the M_W 6.2 earthquake on May 5, 2023, ruptured a different fault segment next to the source fault of the 1993 Off Noto Peninsula earthquake.

Active seismic activity in and around the rupture area of the M_W 6.2 earthquake on May 5, 2023, continued intensively even after this earthquake, and then a devastating earthquake of M_{JMA} 7.6 occurred at 16:10:09 JST on January 1, 2024, as described in Yoshida et al. (2024). The hypocenter of the M_{JMA} 7.6 earthquake was located at the southwestern edge of the asperity of this event (Fig. 8b). The stress concentration produced by the rupture of this asperity may have controlled the rupture initiation of a devastating earthquake. Details of the spatiotemporal rupture process of the M_{JMA} 7.6 event will be reported in a subsequent study.

A brief summary of the above-mentioned seismic activity in and around the source region of the M_W 6.2 earthquake is listed in Table 1.

5 Conclusions

The rupture of the M_W 6.2 earthquake propagated mainly in the up-dip direction on a source fault plane dipping southeastward at a dip angle of 40° with a strike of 49°. This fault geometry did not correspond to the nearby seafloor active fault (NT5), and it was deeper than NT5. Therefore, it was concluded that this earthquake ruptured another blind fault located deeper than NT5. The rupture of the source fault continued for approximately 8 s, and a significant slip was found in the depth range of 8–11 km, which was approximately 4 km in the up-dip direction from the hypocenter. The slip direction was thrust type, with a small right-lateral strike-slip component. The total seismic moment and moment magnitude of the estimated source model were 2.40×10^{18} Nm and 6.2, respectively. The rupture process and final slip distribution correlated well with the V_P/V_S ratio along the dip direction. Particularly, the location of the significant slip corresponded to the region of low V_P/V_S ratio.

The large-slip area is located on the shallower extension of a fault corresponding to the preceding seismic activity occurring primarily at depths from 10 to 14 km, including an M_{JMA} 5.4 event on June 19, 2022. The slip during the M_W 6.2 earthquake is relatively low in the aftershock area of the 2022 M_{JMA} 5.4 earthquake. The seismic activity immediately after this earthquake occurred around

Table 1 List of significant earthquakes in the studied area and their relationship with the M_W 6.2 (M_{JMA} 6.5) earthquake on May 5, 2023

Origin time (JST)	M_{JMA} (M_W)	Latitude (°N)	Longitude (°E)	Depth (km)	Is fault plane same?	Dip direction
1993/2/7 22:27:43.67	6.6	37.641	137.313	14.9	No	Unclear (Northwest or Southeast)
2022/6/19 15:08:07.59	5.4 (5.1)	37.515	137.276	13.1	Yes (Down-dip)	Southeast
2023/5/5 14:42:04.10	6.5 (6.2)	37.539	137.305	12.1	Yes	Southeast
2023/5/5 14:42:33.87	5.4	37.519	137.314	14.6	Yes (Down-dip)	Southeast
2023/5/5 21:58:04.18	5.9 (5.7)	37.526	137.236	13.7	No	Southeast
2024/1/1 16:10:09.54	7.6 (7.5)	37.508	137.230	10.1	Partly Yes (West)	Southeast

Origin time, hypocenter and magnitude are from the JMA Unified Hypocenter Catalog except for the 1993 event, which is from Tsukuda et al. (1994)

the large-slip area, with intensive small earthquakes occurring at shallow depths (< 10 km). Active seismic activity in and around the rupture area of the M_W 6.2 earthquake on May 5, 2023, continued intensively even after this earthquake. The rupture starting point of the 2024 Noto Hanto earthquake (M_{JMA} 7.6) on January 1, 2024, was located at the southwestern edge of the asperity of the M_W 6.2 earthquake. From the above comparison between the source rupture process and the temporal seismic activities, this earthquake can be interpreted as one of turning point in this earthquake swarm activity to connect the preceding swarm in the depth range from 10 to 15 km with seismic activity in shallower depths including the further destructive event.

Abbreviations

ABIC	Akaike's Bayesian Information Criterion
ERI	Earthquake Research Institute
FDM	Finite difference method
HERP	Headquarters for Earthquake Research Promotion
JMA	Japan Meteorological Agency
JIVSM	Japan Integrated Velocity Structure Model
JST	Japan Standard Time
MEXT	Ministry of Education, Culture, Sports, Science, and Technology
MOWLAS	Monitoring of Waves on Land and Seafloor
NIED	National Research Institute for Earth Science and Disaster Resilience
UTC	Coordinated Universal Time

Supplementary Information

The online version contains supplementary material available at https://doi.org/10.1186/s40623-025-02186-w.

Additional file 1: Fig. S1. Bedrock depth and vertical cross section of JIVSM (Koketsu et al. 2012). (Top) Map of bedrock depth corresponding to the top depth at V_S = 3.2 km/s in the FDM model space. The open star indicates the epicenter of the M_W 6.2 earthquake on May 5, 2023, located by JMA. (Bottom) Vertical cross section of the S-wave velocity model of the JIVSM along lines A–A'. The open star indicates the hypocenter of the M_W 6.2 earthquake on May 5, 2023, located by the JMA. Fig. S2. Comparison of simulated Green's functions between forward (black) and reciprocal (red) simulations. Fig. S3. Comparison of synthetic velocity waveforms for three cases with different strike and dip angles (red, green, and blue) and observed velocity waveforms (black) in 0.05–1.0 Hz. Amplitudes were normalized to the maximum observed amplitude of each station. The maximum observed amplitude is shown above each trace in units of cm/s.

Additional file 2: Digital data of the finite source model obtained in this study in ASCII format.

Acknowledgements
Reciprocal Green's functions were computed using the laurel3 supercomputer at the Academic Center for Computing and Media Studies, Kyoto University. All figures were drawn using Generic Mapping Tools v6.5 (Wessel et al. 2019). The authors sincerely appreciated two anonymous reviewers and the guest editor Prof. Yoshihiro Hiramatsu for their constructive comments on our manuscript.

Author contributions
KA analyzed the data and drafted the manuscript. TI participated in the interpretation of the results and discussion. All the authors have read and approved the final version of the manuscript.

Funding
This work was supported by Grant-in-Aid for Special Purposes 23K17482 from MEXT (PI: Prof. Yoshihiro Hiramatsu at Kanazawa University). This study was also supported by the Second and Third Earthquake and Volcano Hazards Observation and Research Programs of MEXT.

Availability of data and materials
Strong-motion waveform data recorded by K-NET and KiK-net (Aoi et al. 2020; NIED 2019b) were provided by the NIED via their websites (https://www.kyoshin.bosai.go.jp/). The strong-motion waveform data recorded by F-net (Aoi et al. 2020; NIED 2019a) and the three-dimensional seismic velocity model of Matsubara et al. (2022) were released from NIED Hi-net website (https://www.hinet.bosai.go.jp/) The strong-motion waveform data of seismic intensity observation networks of Japan Meteorological Agency (JMA) were downloaded from their website (https://www.data.jma.go.jp/eew/data/ltpgm_explain/data/past/past_list.html). Strong-motion waveform data from the seismic intensity observation networks of the Ishikawa Prefecture were provided by the Ishikawa prefectural government. The JIVSM was downloaded from the HERP website (https://www.jishin.go.jp/evaluation/seismic_hazard_map/lpshm/12_choshuki_dat/). The JMA Unified Hypocenter Catalog was published as the Seismological Bulletin of Japan in collaboration with the Ministry of Education, Culture, Sports, Science, and Technology (MEXT) (https://www.data.jma.go.jp/svd/eqev/data/bulletin/index_e.html). The relocated earthquake catalog published by Yoshida et al. (2024) was downloaded from Zenodo (https://doi.org/https://doi.org/10.5281/zenodo.12799165). The 10 m mesh digital elevation model was published in the Digital Map (Basic Geospatial Information) by the Geospatial Information Authority of Japan. SYNBATH V2.0 data grid (Sandwell et al. 2022) was obtained from the Generic Mapping Tools remote data server.

Declarations

Ethics approval and consent to participate
Not applicable.

Consent for publication
Not applicable.

Competing interests
The authors declare that they have no competing interests.

Author details
[1]Disaster Prevention Research Institute, Kyoto University, Gokasho, Uji, Kyoto 611-0011, Japan. [2]Kyoto University, Gokasho, Uji, Kyoto 611-0011, Japan.

Received: 6 October 2024 Accepted: 8 April 2025
Published online: 23 April 2025

References

Akaike H (1980) Likelihood and the Bayes procedure. Trabajos De Estadistica Y De Investigacion Operativa 31:143–166. https://doi.org/10.1007/BF02888350

Amezawa Y, Hiramatsu Y, Miyakawa A, Imanishi K, Otsubo M (2023) Long-living earthquake swarm and intermittent seismicity in the northeastern tip of the Noto Peninsula, Japan. Geophys Res Lett. https://doi.org/10.1029/2022GL102670

Aoi S, Asano Y, Kunugi T, Kimura T, Uehira K, Takahashi N, Ueda H, Shiomi K, Matsumoto T, Fujiwara H (2020) MOWLAS: NIED observation network for earthquake, tsunami and volcano. Earth Planets Space 72:126. https://doi.org/10.1186/s40623-020-01250-x

Asano K, Iwata T (2011) Source-rupture process of the 2007 Noto Hanto, Japan, earthquake estimated by the joint inversion of strong motion and GPS data. Bull Seismol Soc Am 101:2467–2480. https://doi.org/10.1785/0120100254

Asano K, Iwata T (2019) Source rupture process of the 2018 Hokkaido Eastern Iburi earthquake deduced from strong-motion data considering seismic wave propagation in three-dimensional velocity structure. Earth Planets Space 71:101. https://doi.org/10.1186/s40623-019-1080-0

Asano K, Iwata T (2021) Revisiting the source rupture process of the mainshock of the 2016 Kumamoto earthquake and implications for the generation of near-fault ground motions and forward-directivity pulse. Bull Seismol Soc Am 111:2426–2440. https://doi.org/10.1785/0120210047

Asano K, Sekiguchi H, Iwata T, Yoshimi M, Hayashida T, Saomoto H, Horikawa H (2016) Modelling of wave propagation and attenuation in the Osaka sedimentary basin, western Japan, during the 2013 Awaji Island earthquake. Geophys J Int 204:1678–1694. https://doi.org/10.1093/gji/ggv543

Burridge R, Knopoff L (1964) Body force equivalents for seismic dislocations. Bull Seismol Soc Am 54:1875–1888. https://doi.org/10.1785/BSSA05406A1875

Eisner L, Clayton RW (2001) A reciprocity method for multiple-source simulations. Bull Seismol Soc Am 91:553–560. https://doi.org/10.1785/0120000222

Fukahata Y, Wright TJ (2008) A non-linear geodetic data inversion using ABIC for slip distribution on a fault with an unknown dip angle. Geophys J Int 173:353–364. https://doi.org/10.1111/j.1365-246X.2007.03713.x

Gallovič F, Imperatori W, Mai PM (2015) Effects of three-dimensional crustal structure and smoothing constraint on earthquake slip inversions: case study of the Mw 6.3 2009 L'Aquila earthquake. J Geophys Res Solid Earth 120:428–449. https://doi.org/10.1002/2014JB011650

Graves RW, Wald DJ (2001) Resolution analysis of finite fault source inversion using one- and three-dimensional Green's functions: 1. Strong motions. J Geophys Res 106:8745–8766. https://doi.org/10.1029/2000JB900436

Guo Y, Koketsu K, Ohno T (2013) Analysis of the rupture process of the 1995 Kobe earthquake using a 3D velocity structure. Earth Planets Space 65:1581–1586. https://doi.org/10.5047/eps.2013.07.006

Hartzell SH, Heaton TH (1983) Inversion of strong ground motion and teleseismic waveform data for the fault rupture history of the 1979 Imperial valley, California, earthquake. Bull Seismol Soc Am 73:1553–1583. https://doi.org/10.1785/BSSA07306A1553

Hori M, Matsumoto S, Uehira K, Okada T, Yamada T, Ito Y, Shinohara M, Miyamachi H, Takahashi H, Nakahigashi K, Watanabe A, Matsushima T, Matsuwo N, Kanazawa T, Shimizu H (2006) Three-dimensional seismic velocity structure as determined by double-difference tomography in and around the focal area of the 2005 West off Fukuoka Prefecture earthquake. Earth Planet Space 58:1621–1626. https://doi.org/10.1186/BF03352672

Inoue T, Okamura Y (2010) Explanatory notes of 1:200,000 marine geological map around the northern part of Noto Peninsula, Digital Geoscience. Map, S-1. Geological Survey of Japan, Tsukuba

Ishiyama T, Sato H, Kato N, Koshiya S, Abe S, Shiraishi K, Matsubara M (2017) Structures and active tectonics of compressionally reactivated back-arc failed rift across the Toyama Trough in the Sea of Japan, revealed by multiscale seismic profiling. Tectonophysics 710–711:21–36. https://doi.org/10.1016/j.tecto.2016.09.029

Ito M, Kameo K, Satoguchi Y, Masuda F, Hiroki Y, Takano O, Nakajima T, Suzuki N (2016) Neogene-quaternary sedimentary successions. In: Moreno T, Wallis S, Kojima T, Gibbons W (eds) The Geology of Japan. The Geological Society of London, London, pp 309–337

Japan Meteorological Agency (JMA) (2023) The Seismological Bulletin of Japan, Tokyo. https://www.data.jma.go.jp/svd/eqev/data/bulletin/index_e.html. Accessed 21 Aug 2023

Kamata M, Takemura M (1999) Source depth and focal mechanism of the 1993 Noto-Hanto-Oki earthquake and subsurface structures in and around Noto Peninsula derived from Rayleigh waves observed at local stations. Zisin 52:255–270. https://doi.org/10.4294/zisin1948.52.2_255. (**in Japanese with English abstract**)

Kato A (2024) Implications of fault-valve behavior from immediate aftershocks following the 2023 Mj6.5 earthquake beneath the Noto Peninsula, Central Japan. Geophys Res Lett. https://doi.org/10.1029/2023GL106444

Koketsu K, Miyake H, Suzuki H (2012) Japan integrated velocity structure model version 1. In: Proceedings of the 15th world conference on earthquake engineering, Lisbon, 24–28 September 2012

Kubo H, Asano K, Iwata T, Aoi S (2016) Development of fully Bayesian multiple-time-window source inversion. Geophys J Int 204:1601–1619. https://doi.org/10.1093/gji/ggv540

Lawson CL, Hanson RJ (1974) Solving least squares problems. Prentice Hall, Old Tappan

Lee S-J, Liu T-Y, Lin T-C (2023) The role of the west-dipping collision boundary fault in the Taiwan 2022 Chihshang earthquake sequence. Sci Rep 13:3552. https://doi.org/10.1038/s41598-023-30361-0

Ma K-F, Mori J, Lee S-J, Yu SB (2001) Spatial and temporal distribution of slip for the 199 Chi-Chi, Taiwan, earthquake. Bull Seismol Soc Am 91:1069–1087. https://doi.org/10.1785/0120000728

Maruyama T (1963) On the force equivalents of dynamic elastic dislocations with reference to the earthquake mechanism. Bull Earth Res Inst Univ Tokyo 41:467–486. https://doi.org/10.15083/0000033709

Matsubara M, Ishiyama T, No T, Uehira K, Mochizuki M, Kanazawa T, Takahashi N, Kamiya S (2022) Seismic velocity structure along the Sea of Japan with large events derived from seismic tomography for whole Japanese Islands including reflection survey data and NIED MOWLAS Hi-net and S-net data. Earth Planets Space 74:171. https://doi.org/10.1186/s40623-022-01724-0

Mendoza C, Hartzell SH (1988) Aftershock patterns and main shock faulting. Bull Seismol Soc Am 78:1438–1449. https://doi.org/10.1785/BSSA0780041438

Ministry of Education, Culture, Sports, Science and Technology (MEXT), Earthquake Research Institute University of Tokyo (ERI) (2021) Report of the Integrated Research Project on Seismic and Tsunami Hazards around the Sea of Japan

National Research Institute for Earth Science and Disaster Resilience (NIED) (2019a) NIED F-net, Tsukuba. https://doi.org/10.17598/nied.0005

NIED (2019b) NIED K-NET, KiK-net, Tsukuba. https://doi.org/10.17598/nied.0004

Nishimura T, Hiramatsu Y, Ohta Y (2023) Episodic transient deformation revealed by the analysis of multiple GNSS networks in the Noto Peninsula, central Japan. Sci Rep 13:8381. https://doi.org/10.1038/s41598-023-35459-z

Okada T, Hasegawa A, Suganomata J, Umino N, Zhang H, Thurber C (2007a) Imaging the heterogeneous source area of the 2003 M6.4 northern Miyagi earthquake, NE Japan, by double-difference tomography. Tectonophysics 430:57–81. https://doi.org/10.1016/j.tecto.2006.11.001

Okada T, Hasegawa A, Suganomata J, Zhao D, Zhang H, Thurber C (2007b) Imaging the source area of the 1995 southern Hyogo (Kobe) earthquake (M7.3) using double-difference tomography. Earth Planet Sci Lett 253:143–150. https://doi.org/10.1016/j.epsl.2006.10.022

Okada T, Umino N, Hasegawa A, Group for the aftershock observations of the Iwate-Miyagi Nairiku Earthquake in 2008 (2012) Hypocenter distribution and heterogeneous seismic velocity structure in and around the focal area of the 2008 Iwate-Miyagi Nairiku Earthquake, NE Japan—possible seismological evidence for a fluid driven compressional inversion earthquake. Earth Planets Space 64:717–728. https://doi.org/10.5047/eps.2012.03.005

Olson AH, Apsel RJ (1982) Finite faults and inverse theory with applications to the 1979 Imperial valley earthquake. Bull Seismol Soc Am 72:1969–2001. https://doi.org/10.1785/BSSA07206A1969

Sandwell DT, Goff JA, Gevorgian J, Harper H, Kim SS, Yu Y, Tozer B, Wessel P, Smith WHF (2022) Improved bathymetric prediction using geological information: SYNBATH. Earth Space Sci. https://doi.org/10.1029/2021EA002069

Sato H (1994) The relationship between Late Cenozoic tectonic events and stress field and basin development in northeast Japan. J Geophys Res 99:22261–22274. https://doi.org/10.1029/94JB00854

Sato H, Ishiyama T, No T, Kodaira S, Kato N, Claringbould JS, Matsubara M, Hashima A, Ishikawa M, Sato T (2020) Seismogenic source fault models in and around the Sea of Japan. In: Paper presented at Seismological Society of Japan 2020 Fall Meeting, Online, 29–31 October 2020

Sekiguchi H, Irikura K, Iwata T (2000) Fault geometry at the rupture termination of the 1995 Hyogo-ken Nanbu earthquake. Bull Seismol Soc Am 90:117–133. https://doi.org/10.1785/0119990027

Shimomoto K, Kakehi Y (2023) Case study of seismic wave propagation from the earthquakes occurring in the sea area based on numerical simulations. In: Report of Research Center for Urban Safety and Security, vol 27. Kobe University. pp 124–140. https://doi.org/10.24546/0100482524. (**in Japanese**)

Shito A, Matsumoto S, Shimizu H, Ohkura T, Takahashi H, Sakai S, Okada T, Miyamachi H, Kosuga M, Maeda Y, Yoshimi M, Asano Y, Okubo M (2017) Seismic velocity structure in the source region of the 2016 Kumamoto earthquake sequence, Japan. Geophys Res Lett 44:7766–7772. https://doi.org/10.1002/2017GL074593

Somala SN, Ampuero J-P, Lapusta N (2018) Finite-fault source inversion using adjoint methods in 3-D heterogeneous media. Geophys J Int 214:402–420. https://doi.org/10.1093/gji/ggy148
Tsukuda T, Wada H, Sakai K, Ito K (1994) Aftershock distribution of the 1993 M6.6 earthquake off Noto Peninsula and its relation to tectonic features. Bull Earthq Res Inst Univ Tokyo 69:1–18. https://doi.org/10.15083/0000032710
Wald DJ, Heaton TH (1994) Spatial and temporal distribution of slip for the 1992 Landers, California, earthquake. Bull Seismol Soc Am 84:668–691. https://doi.org/10.1785/BSSA0840030668
Wessel P, Luis JF, Uieda L, Scharroo R, Wobbe F, Smith WHF, Tian D (2019) The generic mapping tools version 6. Geochem Geophys Geosyst 20:5556–5564. https://doi.org/10.1029/2019GC008515
Yoshida S, Koketsu K, Shibazaki B, Sagiya K, Kato T, Yoshida Y (1996) Joint inversion of near- and far-field waveforms and geodetic data for the rupture process of the 1995 Kobe earthquake. J Phys Earth 44:437–454. https://doi.org/10.4294/jpe1952.44.437
Yoshida K, Uchida N, Matsumoto Y, Orimo M, Okada T, Hirahara S, Kimura S, Hino R (2023a) Updip fluid flow in the crust of the Northeastern Noto Peninsula, Japan, triggered the 2023 M_w 6.2 Suzu earthquake during swarm activity. Geophys Res Lett. https://doi.org/10.1029/2023GL106023
Yoshida K, Uno M, Matsuzawa T, Yukutake Y, Mukuhira Y, Sato H, Yoshida T (2023b) Upward earthquake swarm migration in the Northeastern Noto Peninsula, Japan, initiated from a deep ring-shaped cluster: possibility of fluid leakage from a hidden magma system. J Geophys Res Solid Earth. https://doi.org/10.1029/2022JB026047
Yoshida K, Takagi R, Fukushima Y, Ando R, Ohta Y, Hiramatsu Y (2024) Role of a hidden fault in the early process of the 2024 Mw 7.5 Noto Peninsula earthquake. Geophys Res Lett. https://doi.org/10.1029/2024GL110993
Yun S, Koketsu K, Kobayashi R (2016) Source process of the 1923 Kanto earthquake considering subduction interface geometry and amplification effects caused by the large scale and 3D complex sedimentary basin. Bull Seismol Soc Am 106:2817–2830. https://doi.org/10.1785/0120150371
Okada T, Umino N, Hasegawa A, Group for the aftershock observations of the Iwate-Miyagi Nairiku Earthquake in 2008 (2012) Hypocenter distribution and heterogeneous seismic velocity structure in and around the focal area of the 2008 Iwate-Miyagi Nairiku Earthquake, NE Japan—possible seismological evidence for a fluid driven compressional inversion earthquake. Earth Planets Space 64:717–728. https://doi.org/10.5047/eps.2012.03.005.

Publisher's Note